IRIS AperTO

UNIVERSITÀ DEGLI STUDI DI TORINO

AperTO - Archivio Istituzionale Open Access dell'Università di Torino

Detecting the stimulated decay of axions at radio frequencies

This is the author's manuscript

Original Citation:

Availability:

This version is available http://hdl.handle.net/2318/1729183 since 2020-02-20T12:48:38Z

Published version:

DOI:10.1088/1475-7516/2019/03/027

Terms of use:

Open Access

Anyone can freely access the full text of works made available as "Open Access". Works made available under a Creative Commons license can be used according to the terms and conditions of said license. Use of all other works requires consent of the right holder (author or publisher) if not exempted from copyright protection by the applicable law.

(Article begins on next page)

12 October 2024

Detecting the Stimulated Decay of Axions at Radio Frequencies

Andrea Caputo[a], **Marco Regis**[b,c], **Marco Taoso**[c], **Samuel J. Witte**[a]

[a] *Instituto de Física Corpuscular, CSIC-Universitat de Valencia, Apartado de Correos 22085, E-46071, Spain*

[b] *Dipartimento di Fisica, Università di Torino, via P. Giuria 1, I–10125 Torino, Italy*

[c] *Istituto Nazionale di Fisica Nucleare, Sezione di Torino, via P. Giuria 1, I–10125 Torino, Italy*

Abstract

Assuming axion-like particles account for the entirety of the dark matter in the Universe, we study the possibility of detecting their decay into photons at radio frequencies. We discuss different astrophysical targets, such as dwarf spheroidal galaxies, the Galactic Center and halo, and galaxy clusters. The presence of an ambient radiation field leads to a stimulated enhancement of the decay rate; depending on the environment and the mass of the axion, the effect of stimulated emission may amplify the photon flux by serval orders of magnitude. For axion-photon couplings allowed by astrophysical and laboratory constraints (and possibly favored by stellar cooling), we find the signal to be within the reach of next-generation radio telescopes such as the Square Kilometer Array.

1 Introduction

The cumulative astrophysical and cosmological evidence for the existence of a non-baryonic, minimally interacting, cold matter component of the Universe (conventionally referred to as dark matter) is overwhelming, with current observations suggesting that dark matter resides in the form of new unknown particles. However, the exact nature of dark matter continues to evade physicists.

The most popular dark matter candidates are those naturally capable resolving additional fundamental problems at the forefront of particle physics. One such candidate is the QCD axion, which inherently appears in the Peccei-Quinn solution to the strong CP problem [1–4][1]. If the mass of the axion is $\lesssim 20$ eV, the axion is stable on cosmological timescales and can contribute substantially to the current fraction of energy density in the Universe stored in form of cold dark matter [5–8]. Astrophysical observations constrain the axion mass to reside approximately between $10^{-4}\,\mu$eV and $10^{4}\,\mu$eV [9, 10] [2]. The mass range where axions can account for the entirety of the dark matter depends on the interplay between different production mechanisms (in particular, the interplay between the misalignment mechanism and the decay of topological defects) and whether the PQ symmetry (i.e. the symmetry introduced in the Peccei-Quinn solution to the strong CP problem) is broken before or after inflation (see e.g. [9, 10] for more extensive discussions). In the post-inflationary PQ breaking scenario, and assuming axions are produced exclusively from the misalignment mechanism, one finds the axion mass $m_a \simeq$ few $\times$ (10) μeV [12]. As we will show, radio telescopes searching for axion decay are ideally placed to probe this mass regime.

In recent years an increasing amount of attention has shifted toward searching for axion dark matter. An important consequence of this has been the development of a diverse and complementary search program intended to probe the many unique facets of such a dark matter candidate; this program includes, but is not limited to, haloscopes [13–17], heliscopes [18–20], 5th force experiments [21–25], light-shinning-through wall experiments [26–31], LC circuit resonators [32–34], oscillating nuclear dipole searches [35–37], axion-induced atomic transitions [38,39], axion-induced atomic and molecular electric dipole moments [40], and indirect axion searches [41–46]. Many of these searches, although certainly not all, rely on the axion's coupling to photons; this interaction is given by the operator $\mathcal{L} = -\frac{1}{4} g_{a\gamma\gamma}\, a\, F_{\mu\nu}\tilde{F}_{\mu\nu}$, where a is the axion field, $F_{\mu\nu}$ is the electromagnetic field strength, $\tilde{F}_{\mu\nu}$ its dual, and $g_{a\gamma\gamma}$ the coupling constant. Of particular importance here is the notion that one may be able to exploit the large number density of axions in astrophysical environments to indirectly infer their existence through the detection of low-energy photons. For axion masses in the 'characteristic' dark matter window (i.e. $\mu\text{eV} \lesssim m_a \lesssim 10^2 \mu\text{eV}$), the energy of a non-relativistic axion corresponds to a photon with a frequency ranging from $\sim \mathcal{O}(100)$ MHz to $\sim \mathcal{O}(10)$ GHz; intriguingly, this lies exactly in the range of frequencies probed by radio telescopes.

There have been various attempts in recent years to use radio telescopes to detect axion dark matter, a majority of which have relied on the axion-to-photon conversion process (i.e. the so-called Primakoff effect). Recently it was shown that unless one exploits a resonant axion-photon conversion (as e.g. was done in [43–45]), the rate of axion decay into two photons will likely supersede that of axion-photon conversion in large-scale astrophysical environments [42, 46]. One of the difficulties with resonant searches is that they rely on a comprehensive understanding of highly uncertain astrophysical environments. An alternative approach with a far more limited dependence on astrophysical uncertainties, albeit at the potential cost of sensitivity, was proposed in [46]. Ref [46] performed an exploratory study for an idealized near future radio telescope to determine whether the axion-to-two-photon decay process could potentially produce an observable signature. This work presented here is intended to serve as a comprehensive follow-up, incorporating a far more sophisticated treatment of near-future radio sensitivity and exploring a variety of

[1] Simply put, the strong CP problem arises from the fact that the QCD θ term predicts a non-vanishing neutron electric dipole moment, while current experimental bounds constrain θ to an unnaturally small value, $\theta \lesssim 10^{-10}$.

[2] However see [11] for models where the astrophysical bounds are relaxed.

astrophysical sources (including the Galactic halo, the galaxy M87 in the Virgo cluster and dwarf spheroidal galaxies). Moreover, this work presents a more detailed treatment of the stimulated emission, a mechanism which is induced by the presence of a background radiation in the medium where the axion decay occurs (see also [47–49]). At low radio frequencies, this effect enhances the expected emission by several orders of magnitude.

The coupling of the QCD axion to the photon $g_{\gamma\gamma}$ grows linearly with the axion mass and with a proportionality constant that depends on the UV completion of the axion model. Considering various types of UV completions thus defines a band in the mass-coupling plane identifying where viable QCD axions may reside (see the light green region in Fig. 2)[3]. More generically, many extensions of the Standard Model predict light particles with similar properties to the QCD axion, but that might not be related to the strong CP problem and for which the relation between $g_{\gamma\gamma}$ and the mass could be different. These are referred to as axion-like particles (ALPs), and they appear generically in low energy-effective theories arising from string theory, e.g. [55–58]. It is therefore important to explore all the parameter space of ALPs, beyond the well-motivated case of the QCD axion.

The results presented here suggest that near-future surveys will be incapable of probing the parameter space of the QCD axion; however we find that the Square Kilometer Array (SKA) will be able to improve current bounds on ALPs by about one order of magnitude.

The paper is organized as follows. Section 2 outlines the origin of stimulated decay and the relevant contributions to the ambient photon background. Section 3 describes how to compute the expected signal-to-noise arising from axion decay for a generic choice of astrophysical environment and radio telescope. We present the sensitivity on the ALP-photon coupling for various astrophysical targets and telescopes in Section 4. In Section 5 we conclude.

2 Axion decay in a photon bath - stimulated emission

The decay of an axion with mass m_a proceeds through the chiral anomaly and produces two photons, each with a frequency $\nu = m_a/4\pi$. The lifetime of the axion can be expressed in terms of its mass and the effective axion-two-photon coupling $g_{a\gamma\gamma}$ as

$$\tau_a = \frac{64\pi}{m_a^3\, g_{a\gamma\gamma}^2}\,. \tag{2.1}$$

Evaluating the lifetime for an axion mass $m_a \sim 1\,\mu\text{eV}$ and a coupling near the current upper limit, i.e. $g_{a\gamma\gamma} \sim 10^{-10}\,\text{GeV}^{-1}$, one finds $\tau_a \sim 10^{32}$ years; this is perhaps the main reason why axion decay has been largely neglected in the literature. The decay rate, however, is only valid in vacuum. In reality, for the axion masses of interest this decay process takes place in an ambient radiation field, which, at radio frequencies is sourced by the combination of cosmic microwave background (CMB) radiation, synchrotron radiation, and bremsstrahlung radiation. Consequently, the photon production rate is enhanced via stimulated emission, a phenomenon due to the indistinguishability of photons and Bose-Einstein statistics. Here we review how to derive the effect in the case of a decay into two photons (for the more canonical decay into a single photon, see, e.g. [59]).

Let us denote a particular phase-space distribution with f, related to the number density of particles n by $dn = \frac{g}{(2\pi)^3}\, f(\mathbf{p})\, d^3p$, with g being the number of degrees of freedom. We consider a initial quantum state where there exist f_a axions with a particular momentum. The final state contains $f_a - 1$ axions and two photons, each with half the energy of the initial axion. The decay occurs in a medium of photons, with f_γ particles with the same momentum and polarization as the photons produced by the axion decay. Therefore, the initial state is $|f_a; f_\gamma; f_\gamma\rangle$ and the final state is $|f_a - 1; f_\gamma + 1; f_\gamma + 1\rangle$. The interaction Hamiltonian in terms of the creation and annihilation

[3] See [50] for a recent determination of the allowed region in the $g_{\gamma\gamma} - m_a$ plane for the KSVZ model [51, 52] and [53, 54] for scenarios where the range of couplings can be further extended.

operators looks like

$$H_{int} = \mathcal{M}_0^\dagger a_\gamma^\dagger a_\gamma^\dagger a_a + h.c. \tag{2.2}$$

where $\mathcal{M}_0$ is related to the spontaneous emission, as will be made clear momentarily. The matrix element associated with the probability of having a transition from initial to final state is:

$$\mathcal{M}_{i\to f} = \langle f_a - 1; f_\gamma + 1; f_\gamma + 1 | H | f_a; f_\gamma; f_\gamma \rangle = \mathcal{M}_0^\dagger \sqrt{f_a}\sqrt{f_\gamma + 1}\sqrt{f_\gamma + 1}. \tag{2.3}$$

where we have used the properties of ladder operators (i.e., $a|f_i\rangle = \sqrt{f_i}|f_i - 1\rangle$ and $a^\dagger|f_i\rangle = \sqrt{f_i + 1}|f_i + 1\rangle$). Squaring the matrix element, one finds

$$|\mathcal{M}_{i\to f}|^2 = |\mathcal{M}_0|^2 \, f_a \, (f_\gamma + 1)^2 \, . \tag{2.4}$$

A similar computation can be performed for the inverse process (i.e. two photons creating an axion in a medium with f_γ photons and f_a axions):

$$\mathcal{M}_{f\to i} = \langle f_a + 1; f_\gamma - 1; f_\gamma - 1 | H | f_a; f_\gamma; f_\gamma \rangle \to |\mathcal{M}_{f\to i}|^2 = |\mathcal{M}_0|^2 \, f_\gamma^2 \, (f_a + 1) \, . \tag{2.5}$$

The variation of the number of axions is just the difference between production (described by Eq. (2.5), which is the term usually identified as the "absorption" term) and decay of axions (given by Eq. 2.4, i.e., the emission term):

$$|\mathcal{M}_{f\to i}|^2 - |\mathcal{M}_{i\to f}|^2 = -|\mathcal{M}_0|^2 \, (f_a + 2 f_a \, f_\gamma - f_\gamma^2) \tag{2.6}$$

The last three terms in the right-hand side of Eq. (2.6) describe the spontaneous decay, stimulated decay, and inverse decay, respectively. Note that the term $\propto f_a \, f_\gamma^2$ cancels out between decay and production. For all environments considered in this work $f_a \gg f_\gamma$, so the inverse decay can be neglected.

The axion decay rate can then be obtained integrating the matrix element over all the momenta (and imposing energy-momentum conservation), leading to the well-known Boltzmann Equation (see e.g. [60]):

$$\begin{aligned} \dot{n}_a &= -\int d\Pi_a d\Pi_\gamma d\Pi_\gamma (2\pi)^4 \, \delta^4(p_a - p_\gamma - p_\gamma) \, |\mathcal{M}_0|^2 \, [f_a \, (f_\gamma + 1)(f_\gamma + 1) + (f_a + 1) \, f_\gamma \, f_\gamma] \\ &= -\int d\Pi_a d\Pi_\gamma d\Pi_\gamma (2\pi)^4 \, \delta^4(p_a - p_\gamma - p_\gamma) \, |\mathcal{M}_0|^2 \, [f_a \, (1 + 2 \, f_\gamma) - f_\gamma^2] \\ &\simeq -n_a \, \Gamma_a \, (1 + 2 \, f_\gamma) \, , \end{aligned} \tag{2.7}$$

where $d\Pi_i = g_i/(2\pi)^3 d^3p/(2\,E)$ and in the last line we used the definition of the decay rate $\Gamma_a = \int d\Pi_\gamma d\Pi_\gamma (2\pi)^4 \, \delta^4(p_a - p_\gamma - p_\gamma) \, |\mathcal{M}_0|^2/(2\,m_a)$.

It should be clear from Eq. (2.7) that the effect of stimulated emission can be incorporated by simply multiplying the rate of spontaneous emission by a factor $2\,f_\gamma$. The photon occupation number f_γ can be obtained from the associated differential energy density of the ambient radiation using $\rho_i(E_i)\,dE_i = d\Pi_i \, 2\,E_i^2 \, f_i$ which leads to:

$$f_\gamma = \frac{\pi^2 \rho_\gamma}{E_\gamma^3}. \tag{2.8}$$

In Fig. 1, we show the stimulated emission factor arising from the CMB (black), Galactic diffuse emission (red), and the extragalactic radio background (green), as a function of the axion mass. Fig. 1 shows that for an axion mass $m_a \sim 1\,\mu$eV, the stimulated decay produces an enhancement by a factor $\gtrsim 10^5$, regardless of the astrophysical environment.

3 Radio Sensitivity

In the following Sections we outline the procedure for computing the expected radio emission from, and the detectability of, axion decay for various astrophysical targets and telescopes. Before beginning, we comment on a number of subtle, but important features of the expected signal. First, the signal is expected to be rather diffuse, at least when compared with the beam of typical radio telescopes. For such a diffuse emission, a relatively large beam is desired in order to enhance the signal-to-noise. This can be easily achieved by single-dish telescopes. On the other hand, their collecting area (and thus the sensitivity) is typically much smaller than that of interferometers (that, in addition, have a smaller synthesized beam). Moreover, larger beams also imply larger foregrounds and larger confusion from background sources. Since it is not obvious *a priori* whether single-dish telescopes or radio interferometers will perform better, we consider results for both observing modes.

In the near future, one of the most powerful radio telescopes available will be the SKA. We consider here a total of five different configurations for SKA [61]. Phase one of SKA-Mid (labeled here as 'SKA1-Mid') will be built and operational as early as 2022. We also consider a configuration of SKA-Mid consistent with the proposed upgrade (labeled here as 'SKA2-Mid'), which has a slightly wider frequency band, 10 times more telescopes, and includes phase array feed (PAF) technology.[4] The analysis below allows both telescopes to operate in either single-dish or interferometric modes. The SKA collaboration has also planned the construction of a low frequency array, which is assumed here to operate solely in the interferometric configuration (note that the synthesized beam increases at small frequencies, and thus the potential tradeoff between interferometric and single-dish observations is reduced significantly). In the coming years, the radio community will begin a significant experimental effort to map large scales at frequencies below 1 GHz in connection to the study of cosmological hydrogen (redshifted 21 cm line). Data collected in these surveys can also be used to search for the signal discussed here. As a reference telescope of this class, we consider the inteferometer HIRAX [62]. Other planned surveys that can be used to this aim involve, among others, the APERTIF, BINGO, CHIME, FAST and Tianlai telescopes (see [63] for a review of forthcoming experiments).

Details of the performances for HIRAX and for the various configurations of SKA considered in this work are summarized in Tab. 1.

The axion signal is expected to appear as a narrow spectral line, broadened by the axion velocity dispersion. For targets in ordinary galaxies, the expected velocity dispersion is $\sim 10^{-3}\,c$, while for dwarf galaxies may be as small as a few km/s (i.e., a few times $10^{-5}\,c$). An experiment hoping to resolve the spectral features of the line would therefore typically require, respectively, $\sim 10^3$ and $\sim 10^5$ frequency channels. This is in full compliance with SKA capabilities, and while the current HIRAX design includes only 1024 channels, there exists however a foreseen possibility to up-channelizing data to a spectral resolution of 1.5 km/s.

3.1 Expected Flux

The flux density, i.e. the power per unit area per unit frequency, from the spontaneous and stimulated decay of an axion is given by

$$S_{decay} = \frac{\Gamma_a}{4\pi\Delta\nu} \int d\Omega\, d\ell\, \rho_a(\ell,\Omega)\, e^{-\tau(m_a,\ell,\Omega)}\, \left[1 + 2 f_\gamma(\ell,\Omega,m_a)\right] , \tag{3.1}$$

where m_a is the axion mass, $\Gamma_a = \tau_a^{-1}$ is the spontaneous decay rate of axions (given by the inverse of Eq. (2.1)), $\rho_a(\ell,\Omega)$ is the axion mass density, $\Delta\nu$ is the width of the axion line, $f_\gamma(\ell,\Omega,m_a)$ is the ambient photon occupation evaluated at an energy $E_\gamma = m_a/2$, and τ is the optical depth.

[4] A PAF consists of an array of receivers that are off-set in the focal plane of the dish and therefore see slightly different parts of the sky. Combining multiple simultaneous beams, an antenna equipped with PAF provides a much larger field-of-view.

	SKA1-Mid	SKA2-Mid	SKA-Low	HIRAX
Freq. [GHz]	0.35-14	0.35-30	0.05-0.35	0.4-0.8
$N_{\rm PAF}$	1	36	1	1
N_{tele}	200	2000	911	1024
D [m]	15	15	35	6
$\theta_{\rm sinth}$ [$'$]	3.6-0.09	3.6-0.04	25.2-3.6	10-5
T_{rcvr} [K]	20	20	40	50

Table 1. Telescope performances and configurations considered in this work. For the case of SKA1-Mid and SKA2-Mid, we consider the array working both in interferometric and single-dish modes.

The integral in Eq. (3.1) should be performed over the solid angle covered by the radio telescope and the line of sight between the source and the location of Earth.

Eq. (3.1) describes an isotropic emission. On the other hand, if the ambient radiation field is anisotropic, then the stimulated axion-decay emission will follow the direction of the ambient radiation (since the photon emitted from stimulated axion-decay is produced in the same quantum state as the ambient photon sourcing the stimulated emission). As it will be clearer in the following, we either consider radiation field that are isotropic up to very good approximation (such as CMB and extragalactic background) or model the ambient photons at the source location by exactly taking only the measured continuum emission, namely, only the photons directed towards us. In other words, we consider photons with the right direction to induce a stimulated emission directed towards our location and therefore our estimate are not affected by possible anisotropies in the considered ambient fields.

It is conventional in radio astronomy to work with effective temperatures rather than flux densities. The observed antenna temperature in a single radio telescope is given by

$$T_{\rm ant} = \frac{A_{\rm eff}\ \langle S \rangle}{2k_b}\,, \tag{3.2}$$

where $A_{\rm eff}$ is the effective area of the telescope, which we set to be $A_{\rm eff} = \eta\, A_{\rm coll}$ where $A_{\rm coll}$ is the physical collecting area of the telescope and η is the efficiency (assumed to be 0.8 for SKA [61] and 0.6 for HIRAX [62]), and $\langle S \rangle$ is the bandwidth-averaged flux density. Throughout this work we take the bandwidth to be equal to that width of the axion line, i.e. $\Delta B = \Delta\nu = \nu_a\, \sigma/c$, where ν_a is the central frequency of the line and σ the velocity dispersion of the dark matter particles.

3.2 Telescope Sensitivities

The minimum (rms) observable temperature for a single telescope and one polarization is given by

$$T_{\rm min} = \frac{T_{\rm sys}}{\sqrt{\Delta B\, t_{\rm obs}}}\,, \tag{3.3}$$

where $t_{\rm obs}$ is the observation time (set to be equal to 100 hours throught this work), ΔB is the bandwidth, and the system temperature $T_{\rm sys}$ is given by $T_{\rm sys} = T_{\rm rcvr} + T_{\rm sky}$. $T_{\rm rcvr}$ is the noise of the receiver, while $T_{\rm sky}(\ell, b)$ is the "sky noise" in the direction of observation. In the case of dSph galaxies, we extracted the temperature $T_{\rm sky}$ at the dSph position from the Haslam map [64]

at 408 MHz and rescaled to other frequencies with a spectral index of -2.55. In the cases of the Galactic center and M87, we considered the temperature derived by the same observations we used to describe the radiation field in the context of computing the stimulated emission, see below. Finally, in the case of the Galactic halo, we adopt a sky-average value $T_{\rm sky} \simeq 60\,(\lambda/{\rm m})^{2.55}$ K [61], since we are considering a very large fraction of the sky.

Transitioning from Eq. (3.2) and Eq. (3.3) to observable signal-to-noise of a telescope or an array depends inherently the mode of observation, i.e. interferometric or single-dish observation. The field of view (FoV) can be computed similarly in the two cases, while angular resolution and sensitivity have to be treated separately.

3.3 Field of view

The angle corresponding to the full-width at half maximum (FWHM) of the primary beam is given by

$$\theta_{pb} \simeq 1.22\,\frac{\lambda}{D} \simeq 0.7^\circ \left(\frac{1\,{\rm GHz}}{\nu}\right)\left(\frac{15\,{\rm m}}{D}\right), \tag{3.4}$$

where λ and ν are the wavelength and frequency of observation, and D is the diameter of the dish/station. Here, we consider the primary beam area to be $\Omega_{pb} = 2\pi\,(1-\cos(\theta_{pb}/2))$. In the cases of SKA1-Mid, SKA-Low and HIRAX, the FoV is set by the primary beam, i.e. FoV $= \Omega_{pb}$.

The FoV can be however enlarged by equipping the interferometer with PAF technology, which makes FoV $= N_{PAF}\,\Omega_{pb}$, with N_{PAF} expected to be $\gtrsim 36$ for next generation radio telescopes [61]. This is the picture we consider for SKA2-Mid and in this case the signal-to-noise ratio becomes

$$\left(\frac{S}{N}\right)^{PAF} = \sqrt{\sum_{i=1}^{N_{PAF}} \left(\frac{S}{N}\right)^2_{b_i}} \tag{3.5}$$

where $(S/N)_{b_i}$ is the signal-to-noise in the beam i and there are N_{PAF} beams in the FoV. For a spatially uniform emission, the increase of the FoV due to PAF would lead to an increase of the signal-to-noise by a factor of ten.

3.4 Single-dish angular resolution and sensitivity

For single-dish telescopes, the angular resolution is set by Eq. (3.4). The latter defines the integration angle to be used in Eq. (3.1), which leads (through Eq. 3.2) to a certain $T^{\rm pb}_{\rm ant}$. The signal-to-noise ratio for a single telescope and one polarization is simply given by the ratio between Eq. (3.2) and Eq. (3.3):

$$\left(\frac{S}{N}\right)_{sd,{\rm single}} = \frac{T^{\rm pb}_{\rm ant}}{T_{\rm min}}\,. \tag{3.6}$$

Clearly the actual temperature measured by the telescope will not just include the emission associated to axion decay, but also a number of other Galactic or extragalactic radio sources. We assume to be able to remove the continuum ("smooth") radiation, since the telescope considered in this work have a large number of frequency channels that can be used to constrain the spectrum. For a discussion about foreground removal, see, e.g., [65, 66]. On top of that, if the continuum emission is also spatially smooth, like in the direction of dSphs (since they are not expected to source a significant continuum emission, see, e.g., [67]), the foreground does not even enter interferometric observations which are blind to large scales. Therefore, the case of interferometric observations of dSph can be considered the most solid scenario for what concerns foreground removal.

The presence of spectral lines would instead constitute an irreducible background (in particular, if the width is comparable to the width of the axion line). However, there are only a very

limited number of radio lines in the frequency range of interest. The only potentially problematic spectral line is the redshifted 21-cm line, which is relatively bright at low redshifts. The observed frequency scales as $\nu_{obs} = \nu_{em}/(1+z)$ and the emission stays significant up to approximately $z \lesssim 5$. Therefore, it affects the possible detection of axions with masses between about 2-12 μeV. This range is however already strongly constrained by haloscopes except for a narrow window around 3-4 μeV (see Fig. 2). To study potential technical ways to remove such a background (exploiting e.g. different line width and morphology of the axion signal) is beyond the goal of this paper.

Considering an array with $N_{\rm tele}$ telescopes observing in single-dish mode, the signal-to-noise is given by

$$\left(\frac{S}{N}\right)_{sd,\rm array} = \sqrt{N_{\rm tele}\, n_{\rm pol}} \left(\frac{S}{N}\right)_{\rm single} = \sqrt{N_{\rm tele}\, n_{\rm pol}}\, \frac{T_{\rm ant}^{\rm pb}}{T_{\rm min}}\,, \tag{3.7}$$

where $n_{\rm pol}$ is the number of polarizations (we set $n_{\rm pol} = 2$). Finally, for an array equipped with PAF the signal-to noise is simply

$$\left(\frac{S}{N}\right)^{PAF}_{sd,\rm array} = \sqrt{N_{\rm tele}\, n_{\rm pol}} \sqrt{\sum_{b=1}^{N_{PAF}} \left(\frac{T_{\rm ant}^{b}}{T_{\rm min}}\right)^2}\,, \tag{3.8}$$

where $T_{\rm ant}^{b}$ is the antenna temperature in the beam b.

3.5 Angular resolution and sensitivity of interferometers

In a radio interferometer, the angular resolution is set by the longest baseline $b_{\rm max}$, i.e. $\theta_{\rm res} \simeq 1.22\,\lambda/b_{\rm max}$, while the largest scale that can be imaged is set by the shortest baseline $b_{\rm min}$, i.e. $\theta_{\rm max} \simeq 1.22\,\lambda/b_{\rm min}$. The actual synthesized beam and largest observable scale depends also on observational details, such as the coverage in the visibility plane. The emissions discussed here have a typical size $\lesssim \theta_{\rm max}$ for all telescopes, so it is reasonable to assume that there is no flux lost by the interferometric observations, except possibly for high frequencies and extended targets (cases for which we will consider single-dish observations, see Sec. 4). The synthesized beam is determined by considering an "average" baseline, leading to the values of $\theta_{\rm sinth}$ detailed in Table 1. The signal in each "pixel" is the integral of Eq. (3.1) over the synthesized beam, which provides $T_{\rm ant}^{\rm sb}$ (again through Eq. (3.2)).

Considering an array with $N_{\rm tele}$ telescopes operating in an interferometric mode, there are $N_{\rm tele}(N_{\rm tele}-1)/2$ independent baselines, the signal-to-noise given by

$$\left(\frac{S}{N}\right)_{if,\rm array} = \sqrt{\frac{1}{2} N_{\rm tele}(N_{\rm tele}-1)\, n_{\rm pol}} \sqrt{\sum_{pix=1}^{N_{pix}} \left(\frac{T_{\rm ant}^{pix}}{T_{\rm min}}\right)^2}\,, \tag{3.9}$$

where N_{pix} is the number of synthesized beams contained in the area of the primary beam. For a spatially uniform emission, the signal-to-noise is increased by a factor $\sqrt{N_{pix}}$ in the limit that the synthesized beam is equal to the primary beam.

To compute $\left(\frac{S}{N}\right)^{PAF}_{if,\rm array}$, one can again apply Eq. (3.5).

3.6 Radiation Fields for Stimulated Emission

As discussed in Sec. 2, the presence of a non-negligible photon background with the same energy as that produced in the axion decay implies a stimulated enhancement of the axion decay rate; this effect manifests in terms of a non-zero contribution to f_γ in Eq. (3.1). In general, f_γ will be a linear combination over the sources which contribute to the photon bath. At radio frequencies, this

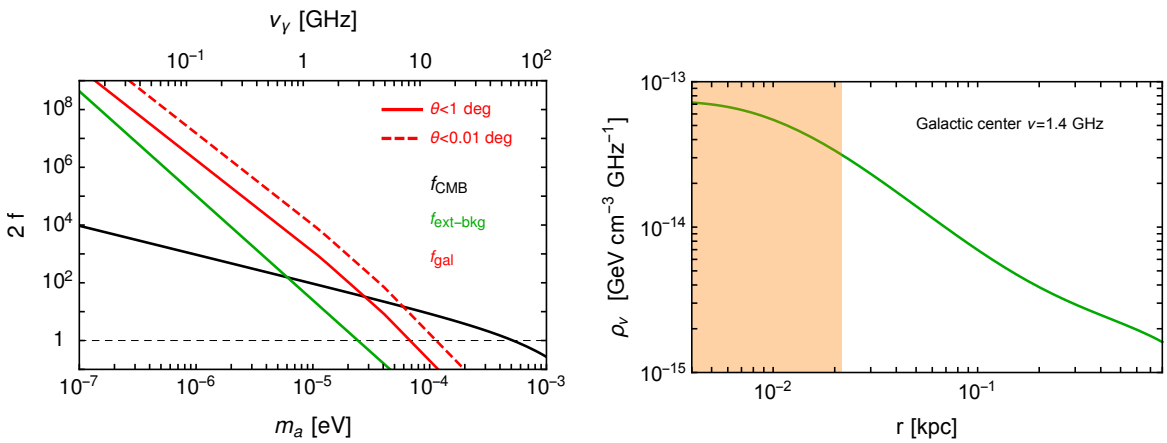

Figure 1. Left: Stimulated emission factor ($2\,f_\gamma$) broken down in terms of contributions from the CMB, the extragalactic radio background, and Galactic diffuse emission. The Galactic contribution is averaged in a region of angular radius of 1 and 0.01 degrees about the Galactic center, see Eq. (4.8). Right: Differential photon energy density at $\nu = 1.4$ GHz as a function of the distance from the Galactic Center.

includes, but is not limited to[5], photons from the cosmic microwave background (CMB), diffuse emission from within the galaxy under consideration, and the radio background from extragalactic sources, i.e. we assume

$$f_\gamma(\ell, \Omega, m_a) \simeq f_{\gamma,\mathrm{CMB}}(m_a) + f_{\gamma,\mathrm{gal}}(\ell, \Omega, m_a) + f_{\gamma,\mathrm{ext-bkg}}(m_a)\,, \tag{3.10}$$

where the spatial dependence of f_γ appears exclusively in the contribution from galactic emission, while $f_{\gamma,\mathrm{CMB}}$ and $f_{\gamma,\mathrm{ext-bkg}}$ are (at first approximation) isotropic.

The photon occupation from a blackbody spectrum is given by

$$f_{\gamma,bb} = \frac{1}{e^x - 1} \qquad x \equiv \frac{E_\gamma}{k_b T} \tag{3.11}$$

where k_b is Boltzmann's constant and T is the blackbody temperature. Eq. (3.11) can be used to incorporate the contribution to f_γ from the CMB, taking $T = 2.725$ K.

For the galactic diffuse and the extragalactic contributions we use Eq. (2.8), namely, we derive the stimulated enhancement factor from the measured radio intensity. The extragalactic radio background has been measured [68,69] to have a frequency-dependent temperature given by

$$T_{\mathrm{ext-bkg}}(\nu) \simeq 1.19 \left(\frac{\mathrm{GHz}}{\nu}\right)^{2.62} \mathrm{K}\,. \tag{3.12}$$

The contribution to f_γ from galactic diffuse emission will be instead specified for each target (Galactic center, M87, Galactic halo) in the next Section. Its spatial dependence is computed from the angular profile of the measured radio flux.

4 Results

Below we present the projected sensitivity contours in the ALP parameter space for different astrophysical targets. For the SKA-Mid, we considered the telescope operating both in single-dish and interferometric modes. These two configurations lead to similar results for the Galactic center and

[5]It is worthwhile to note that at high-frequencies, free-free emission in hot and high-density environments may become the dominant contribution to f_γ. This contribution is neglected in this work.

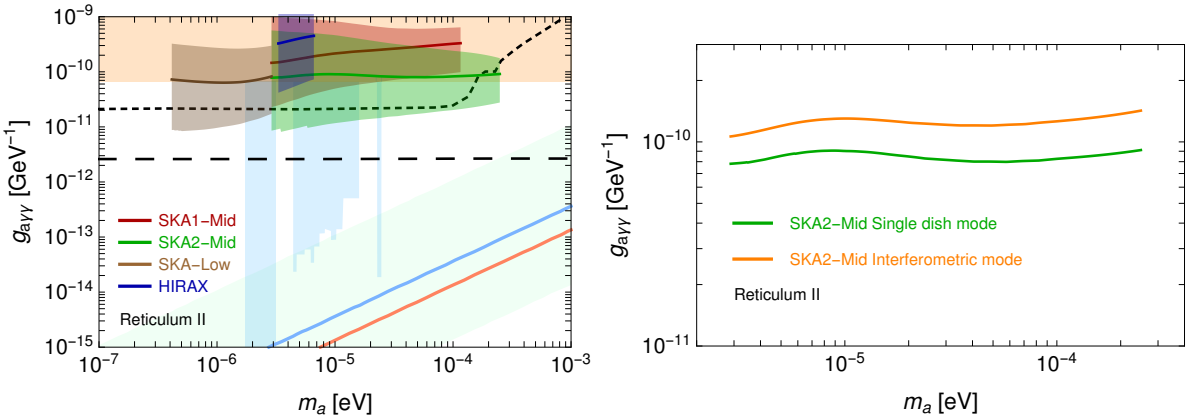

Figure 2. Left panel: Projected sensitivities for the Reticulum II dwarf galaxy. Results are displayed alongside current bounds from haloscopes (light blue) [14–17] and helioscopes (orange) [18], projected bounds from ALPS-II [70] (black, short dashed) and IAXO [19, 20] (black, long dashed), and benchmark QCD axion models (light green band, blue line, orange line) [50]. The width of the expected exclusion contours reflect the astrophysical uncertainty in the dSph environment. Right panel: Comparison between the sensitivites of interferometric and single-dish observations for the Reticulum II dwarf galaxy, considering the SKA2-Mid configuration.

dwarf spheroidal galaxies and we quote only the sensitivities from single-dish observations. This is because in the high-frequency end, the largest scale that can be imaged by the interferometer becomes comparable/smaller than the size of the source, so there might be some loss of flux (that we are not including in the modeling), which does not happen in the case of single-dish observations. At lower frequencies, observational beams become larger, and SKA-Low and HIRAX do not face above issue. For M87 instead, SKA-Mid operating in interferometric mode provides significantly better sensitivities, therefore we show the results only for this configuration. Given the distance from us and the large stimulated emission factor in the central region of the galaxy, the emission from M87 is more compact than in the case of the Galactic center and dwarf spheroidal galaxies. This explains why the interferometric mode, which has a better rms sensitivity and a smaller smaller synthesized beam, is favored with respect to the single-dish mode.

4.1 Dwarf galaxies

As a first target we consider dwarf spheroidal galaxies, refining the analysis performed in [46]. Dwarf spheroidal galaxies offer large dark matter densities, a low velocity dispersion and their angular size is within the field of view of the radio telescopes that we are considering. These properties make them prime targets for searches of radio emissions produced by the decay of axions. The signal, as shown in Eq. (3.1), depends on the integral of the dark matter density distribution in the region of observation, the so-called D-factor $D(\theta)$:

$$D(\theta) = \int d\Omega \, dl \, \rho_a(l, \Omega), \tag{4.1}$$

with θ the angular distance from the center of the the dwarf galaxy. A significant effort is ongoing to reconstruct the D-factors from stellar kinematical observations, see for example [71–76]. Here we make use of the publicly available data in [72, 73], which provide the median values of the D-factors and their uncertainty intervals for several dwarf galaxies. In particular we focus on Reticulum II, which is one of the most promising dwarf galaxies that can be observed by radio telescopes located in the southern hemisphere, like SKA and HIRAX. Similar D-factors have been reported also for other observable (by southern located telescopes) dwarf spheroidal galaxies, both classical (e.g. Sculpture) and ultrafaint (e.g. Coma).

The dark matter velocity dispersion is estimated from the measured stellar velocity dispersion which we take to be $\sigma \simeq 4$ km s^{-1}, see [73]. The uncertainty on σ affects the results mildly, since the sensitivity on $g_{a\gamma\gamma}$ scales as $\sigma^{-1/4}$. For the stimulated emission, we include only the contributions from the CMB and the extragalactic radiation, neglecting any (currently undetected, and likely subdominant) radio emission produced inside the dwarf galaxy.

We show our results in the left panel of Fig. 2. The bands refer to the 95% credibility interval on the D-factor provided in [73]. Under the stated assumptions future radio telescopes might be able to probe a currently unexplored region of the parameter space, corresponding to $g_{a\gamma\gamma} \gtrsim 10^{-11}$ GeV^{-1}.

In Fig. 2 (right), we compare the results of single-dish versus inteferometric observing modes for the SKA2-Mid configuration. As clear from the plot, the difference is limited. For what said in Sec. 3.4, this also shows that the main conclusion of this paper should be not affected by the removal of the continuum emission.

The sensitivity reported in this work differs by about three orders of magnitude (about a factor of 30 in the axion-photon coupling) with respect to [46]. That work applied the SKA interferometric sensitivity as if the source were point-like rather than extended as instead we consider in Eq. (3.9). Moreover, they considered an optimistic SKA collecting area which is not currently foreseen in the future SKA design (i.e., $A_{eff}/T_{sys} = 10^5 \mathrm{m}^2/\mathrm{K}$ at high-frequency, about one order of magnitude larger than our SKA-2 case).

4.2 Galactic center

Due to the close proximity and high dark matter column density, the Galactic center is typically among the most promising targets for indirect dark matter searches. Additionally, the presence of a large synchrotron background is expected to lead to a significant enhancement of the decay rate of axions. We describe the details and caveats of this calculation below.

The distribution of dark matter in the Galactic center, and in particular the inner slope of the density profile, remains largely unknown. N-body simulations of collisionless cold dark matter predict density profiles well-modeled by a Navarro-Frenk-White (NFW) profile [77], in which $\rho(r) \propto r^{-1}$ at small radii. However, mechanisms have been proposed which can either flatten or steepen the distribution to produce a core or cusp. In an attempt to account for this source of uncertainty, we present sensitivity studies for three distinct profiles, one 'reference' distribution, and two profiles intended to characterize the relative extremes. The reference distribution that we consider is the NFW profile:

$$\rho(r) = \frac{\rho_s}{\left(\frac{r}{r_s}\right)\left(1+\frac{r}{r_s}\right)^2}\,, \tag{4.2}$$

where we take a scale radius $r_s = 24.42$ kpc [78] and ρ_s is normalized in order to obtain a density at the Earth's location ($r_\odot = 8.3$ kpc) $\rho(r_\odot) = 0.3\,\mathrm{GeV/cm^3}$. For the more optimistic scenario we consider a cuspy distribution, given by a generalized NFW profile

$$\rho(r) = \frac{\rho_s}{\left(\frac{r}{r_s}\right)^\gamma\left(1+\frac{r}{r_s}\right)^{3-\gamma}}\,, \tag{4.3}$$

with r_s and ρ_s defined as before, and an inner slope γ taken to be 1.3. To model the cored dark matter density profile we adopt the so-called Burkert profile, given by

$$\rho(r) = \frac{\rho_s}{\left(1+\frac{r}{r_{sb}}\right)\left(1+\frac{r}{r_{sb}}\right)^2}\,, \tag{4.4}$$

where $r_{sb} = 12.67$ kpc [78], and as before the scale density is set to provide the reference local density $\rho(r_\odot)$.

The velocity dispersion of dark matter, characterizing the width of the decay line, is taken to be $\sigma = 200$ km/s. To estimate the Galactic contribution to f_γ in Eq. (3.10) the morphology of the radio diffuse emission should be taken into account. Here, we attempt to infer the value and spatial dependence of $f_{\gamma,\rm gal}$ from the measurements of the radio flux in the Galactic center region presented in [79]. Specifically, we analyze the radial profile at $\nu_* = 1.415$ GHz derived by averaging the emission in elliptical annuli (with aspect ratio of two-to-one), located around the Galactic center. To simplify the analysis, we assume that the flux observed in [79], extending up to an angular scale of one degree along the semi-major axis, can be mapped onto a spherically symmetric region, i.e. a circle rather than elliptic annuli, of equivalent area. The observed flux at Earth from a spherically symmetric emissivity $j(r)$ is given by

$$I(\theta) = \frac{1}{4\pi} \int ds\, j(\hat{r}(\theta, s, r_\odot))\,, \tag{4.5}$$

where the line-of-sight coordinate s is related to the radial distance from the Galactic center $\hat{r} = \sqrt{s^2 + r_\odot^2 - 2\, s\, r_\odot \cos(\theta)}$ and θ is the aperture angle from the line-of-sight and the Galactic center direction. For the small angles θ under consideration, one can perform an Abel transform to infer the value of $j(r)$ from the value of $I(\theta)$ provided in [79]. Then, once the emissivity profile has been obtained, one can compute the differential photon density (at the frequency ν_*) as a function of the distance r from the Galactic center:

$$\rho_\nu(r) = \frac{1}{4\pi} \int ds\, d\Omega\, j(\hat{r}(\theta, s, r))\,. \tag{4.6}$$

The resulting distribution is shown in the right panel of Fig. 1. The intensity profile $I(\theta)$ in [79] flattens at small values of θ, an effect due to the finite angular resolution ($539''$) of the observations. In Fig. 1, the corresponding range of Galactic distances r is shaded: in that region the $\rho_\nu(r)$ distribution is likely to be steeper than reported, but we conservatively choose not to extrapolate it. The $\rho_\nu(r)$ is instead extrapolated as r^{-2} at large distances, beyond the range covered by the observations. We checked that our results do not depend on the specific prescription adopted. Finally, it is then straightforward to obtain the photon occupation number $f_{\gamma,\rm gal}(r,\nu)$ from the density distribution $\rho_\nu(r)$. The frequency dependence of the occupation number can be obtained from the observed spectral shape of the emission. From Table 1 of [79] we obtain:

$$f_{\gamma,\rm gal}(r,\nu) = f_{\gamma,\rm gal}(r)\Big|_{\nu=\nu_*} \times \begin{cases} (\nu/\nu_*)^{-3.173} & \nu < \nu_* \\ (\nu/\nu_*)^{-3.582} & \nu_* \leq \nu \leq 4.85\,\text{GHz} \\ 0.49 \times (\nu/\nu_*)^{-4.14} & \nu > 4.85\,\text{GHz} \end{cases}\,. \tag{4.7}$$

The contribution of $f_{\gamma,\rm gal}$ to the stimulated emission is presented in the left panel of Fig. 1. We show the average value in a region of 1 and 0.01 degrees around the Galactic center, defined as:

$$\bar{f}_{\gamma,\rm gal} = \frac{\int d\Omega\, d\ell\, \rho_a(\ell,\Omega)\, f_\gamma(\ell,\Omega,m_a)}{\int d\Omega\, d\ell\, \rho_a(\ell,\Omega)} \tag{4.8}$$

The Galactic contribution dominates over the CMB and extragalactic ones in a large range of frequencies.

The free-free self absorption becomes relevant only at frequencies $\nu \lesssim 10 - 20$ MHz for observations of targets located above the Galactic plane, as dwarf galaxies, and so can be neglected for our purposes. Instead, the emission of sources located at low Galactic latitudes is significantly absorbed already at $\nu \lesssim 200$ MHz, because of the large column density of electrons lying in the Galactic plane. We need to incorporate this effect in our analysis of the Galactic center. We compute the optical depth τ in Eq. (3.1) using [80] and setting a kinetic temperature of 5000 K and

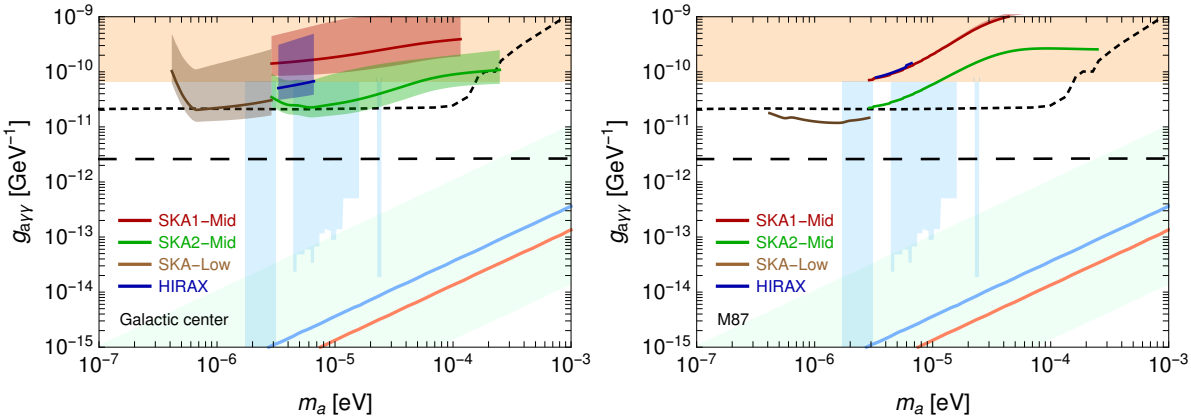

Figure 3. Same as Fig. 2 but for Galactic center (left) and M87 (right).

an emission measure $EM = 10^4$ cm^{-6} pc. The impact of absorption in our results, presented in the left panel of Fig. 3, can be easily recognized: the sensitivity quickly degrades moving towards low frequencies. Overall, the sensitivity reach that we obtain is similar to the one found in Sec. 4.1 for dwarf spheroidal galaxies.

4.3 M87

Given its position in the sky, mass, and distance, the Virgo cluster is likely to be among the most promising galaxy clusters in the search for axion decay. The massive elliptical galaxy M87 lying at its center accounts for a significant fraction of the Virgo mass ($\simeq 5 - 10\%$), and it is a bright radio emitter. An intra-cluster large scale radio halo is much fainter [81]. We checked that M87 provides stronger constraints on ALP parameter space than the Virgo intra-cluster medium. This is because the former hosts a large density of radio photons, leading to a large stimulated emission. In the following we show results only for M87.

To obtain the contribution to the stimulated emission from the diffuse radiation in M87, $f_{\gamma,\mathrm{gal}}(r,\nu)$ in Eq. (3.10), we proceed as follows. The total power radiated by M87 from 10 MHz up to 150 GHz is $L_\gamma = 9.6 \times 10^{41}$erg/s, and it is predominantly produced within $r_p = 40$ kpc of the center of the galaxy [82]. The photon energy density ρ can be estimated simply as $\rho = \frac{L_\gamma\, r_p}{V\, c}$ with $V = \frac{4}{3}\pi r_p^3$. Then, using a spectral dependence of the flux $\propto \nu^{-1}$ [82], one can infer the photon energy density, and thus the occupation number $f_{\gamma,\mathrm{gal}}(r,\nu)$, at any frequency. For simplicity we consider a constant photon distribution inside r_p, with an average value estimated as explained above, and an abrupt depletion of the photon density outside this region.

The dark matter density distribution is modeled using the results of [83], where the mass density has been inferred by jointly analyzing the dynamics of stars, globular clusters, and satellites. In particular, we consider two density distributions, the NFW profile and a cored profile (cgNW in [83]). Finally we caution that we do not attempt to model any absorption inside M87. On the other hand, this can have an impact on both the derived energy density of background photons and the estimated axion-induced flux, with the two effects expected to be of similar size.

The sensitivities are shown in Fig. 3 (right). The changes due to the different choice of dark matter density profile are modest. The two adopted profiles differ little at the distances corresponding to the angular scales under examination.

4.4 Wide field surveys

One of the primary goals of HIRAX is to observe the large-scale structure of the Universe through the 21 cm emission line produced by the neutral hydrogen, the so-called hydrogen intensity map-

ping. For this purpose HIRAX has been designed to measure a large fraction of the sky (1.5×10^4 squared degrees) with a fairly large integrated time (10^4 hours) [62]. We investigate whether the same observational campaign can be used to search for radio lines produced by the decay of axions inside the Galactic halo. We estimate the sensitivity of HIRAX, approximating the region of observation with a circle centered at the Galactic center and spanning an equal area (i.e. 1.5×10^4 squared degrees). The signal is computed assuming the NFW density profile in Sec. 4.2 and a velocity dispersion $\sigma \simeq 200$ km/s. To model the stimulated emission, in Eq. (3.10) we incorporate the sum of the Galactic and extragalactic contribution using $T_{\rm sky}$ described in Sec. 3.2 as a measure of the total radio flux.

We find that the reach is at the level of the region already excluded by haloscopes, namely $g_{a\gamma\gamma} \simeq 8.6 - 17 \times 10^{-11}\,\text{GeV}^{-1}$ in the mass range $m_a \simeq 3.3 - 6.7\,\mu$eV. We have obtained similar sensitivities for the CHIME telescope [84], which will perform a complementary survey of the northern sky.

These estimates, although involving several approximations (namely the patch of the sky which will actually be observed, and the modeling of $f_{\gamma,\rm gal}(r,\nu)$), are enough to conclude that the strategies considered in the previous Sections, i.e. observations of the Galactic center, dwarf galaxies and galaxy clusters, are more promising to look for the decay of axions.

The cumulative line emission from all dark matter halos at all redshifts forms a nearly isotropic emission with a continuum spectrum. We find the cosmological emission to be $\lesssim 10^{-4}$ of the measured extragalactic background (for couplings in the allowed range). Since this collection of lines determines a contribution with no prominent spatial or spectral features, it can be very complicated to identify. A potentially interesting way to overcome this issue is given by line-intensity mapping [85]. We postpose a dedicated analysis of this approach to future work.

4.5 Discussion

The main goal of this work was to study the observability of the two-photon decay of ALPs, with the QCD axion used as a very well-motivated benchmark. More generally, our results apply to any scenario in which a light dark matter candidate (with mass in the range $0.1 - 100\,\mu$eV) has a monochromatic decay to one or two photons. For instance, one could extend the ALP model that we have analyzed, supplementing the Lagrangian by a term $a\,F^{\mu\nu}\tilde{F}'_{\mu\nu}$, where $\tilde{F}'_{\mu\nu}$ is the dual of a new field strength tensor arising from a dark $U(1)$ gauge symmetry [86–90]. Here, if the mass of the dark photon is less than the mass of the axion, the axion decay will proceed via $a \to \gamma\gamma'$ (this model has beed studied e.g. in [91–94]).

For sake of generality, in Fig. 4 we present our sensitivities in terms of the ALP lifetime; these results can then be easily recast for alternatively models. The sensitivity curve is plotted as a function of the ALP mass. For the decay into two photons, we show the best sensitivity from Figs 2 and 3. For the decay into a photon plus a lighter state X, we recast the sensitivity using the relation $E_\gamma = \frac{m_a}{2}\left(1 - \frac{m_X^2}{m_a^2}\right)$ and we show two cases: $m_X = 0$ and $m_X = 0.9\,m_a$. Remarkably, Fig. 4 shows that it may be possible to probe lifetimes as large as 10^{46} seconds.

5 Conclusions

In this work we studied the radio emission arising from axion decays in various types of nearby astrophysical structures. We have presented projected sensitivities for targets with the best observational prospects, including the Galactic center, the ReticulumII dwarf galaxy, M87, and the Galactic halo. We have found that for ALPs with masses below meV, the stimulated decay arising from the presence of ambient photons results in a large enhancement of the decay rate – potentially up to eight orders of magnitude for axion masses $\sim \mu$eV and in environments with large radio emission like the Galactic Center.

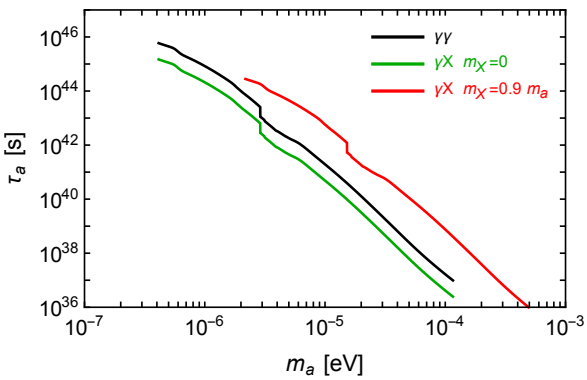

Figure 4. Projected sensitivity from Figs. 2 and 3, translated into constraints on the ALP lifetime as a function of the ALP mass. We show the cases of decays into two photons (black) and into a photon plus a state X, massless (green) or with $m_X = 0.9\, m_a$ (red).

Once the axion mass and the coupling to photons are fixed, the main uncertainty comes from the dark matter distribution in the structure under consideration. Indeed, the effect of stimulated emission can be well determined since the distribution of ambient photons can be confidently derived from continuum radio measurements. This is different from the possible signal coming from photon-axion conversion in strong magnetic fields around stars, which is potentially more promising but suffers of larger uncertainties associated with the poorly known astrophysics (namely the structure of the magnetic field and the plasma density).

We have showed that with near-future radio observations by SKA, it will be possible to increase sensitivity to the ALP-photon coupling by nearly one order of magnitude. Interestingly, it has been shown that in this range of parameter space, axions provide a viable solution to a non-standard cooling mechanism identified in various stellar systems [95]. If forthcoming axion search experiments, such as ALPS-II and IAXO, find a signal consistent with axion dark matter in the $10^{-7} - 10^{-3}$ eV mass range, the technique proposed here might become the standard route to understand the properties of dark matter, such as e.g. its spatial distribution and clustering in cosmological structures.

Acknowledgments

We thank S. Camera, J. Fonseca, N. Fornengo, P. Serpico and M. Viel. MR acknowledges support by "Deciphering the high-energy sky via cross correlation" funded by Accordo Attuativo ASI-INAF n. 2017-14-H.0 and by the "Departments of Excellence 2018 - 2022" Grant awarded by the Italian Ministry of Education, University and Research (MIUR) (L. 232/2016). MR and MT acknowledge support from the project "Theoretical Astroparticle Physics (TAsP)" funded by the INFN. AC and SW acknowledge support from the European projects H2020-MSCAITN-2015//674896-ELUSIVES and H2020-MSCA-RISE2015.

References

[1] R. D. Peccei and Helen R. Quinn. CP Conservation in the Presence of Instantons. *Phys. Rev. Lett.*, 38:1440–1443, 1977. [,328(1977)].

[2] R. D. Peccei and Helen R. Quinn. Constraints Imposed by CP Conservation in the Presence of Instantons. *Phys. Rev.*, D16:1791–1797, 1977.

[3] Steven Weinberg. A New Light Boson? *Phys. Rev. Lett.*, 40:223–226, 1978.

[4] Frank Wilczek. Problem of Strong p and t Invariance in the Presence of Instantons. *Phys. Rev. Lett.*, 40:279–282, 1978.

[5] John Preskill, Mark B. Wise, and Frank Wilczek. Cosmology of the Invisible Axion. *Phys. Lett.*, B120:127–132, 1983. [,URL(1982)].

[6] Michael Dine and Willy Fischler. The Not So Harmless Axion. *Phys. Lett.*, B120:137–141, 1983. [,URL(1982)].

[7] L. F. Abbott and P. Sikivie. A Cosmological Bound on the Invisible Axion. *Phys. Lett.*, B120:133–136, 1983. [,URL(1982)].

[8] Richard Lynn Davis. Cosmic Axions from Cosmic Strings. *Phys. Lett.*, B180:225–230, 1986.

[9] David J. E. Marsh. Axions and ALPs: a very short introduction. In *Proceedings, 13th Patras Workshop on Axions, WIMPs and WISPs, (PATRAS 2017): Thessaloniki, Greece, 15 May 2017 - 19, 2017*, pages 59–74, 2018, 1712.03018.

[10] Igor G. Irastorza and Javier Redondo. New experimental approaches in the search for axion-like particles. 2018, 1801.08127.

[11] Luca Di Luzio, Federico Mescia, Enrico Nardi, Paolo Panci, and Robert Ziegler. Astrophobic Axions. *Phys. Rev. Lett.*, 120(26):261803, 2018, 1712.04940.

[12] Sz. Borsanyi et al. Calculation of the axion mass based on high-temperature lattice quantum chromodynamics. *Nature*, 539(7627):69–71, 2016, 1606.07494.

[13] C. Hagmann, P. Sikivie, N. S. Sullivan, and D. B. Tanner. Results from a search for cosmic axions. *Phys. Rev.*, D42:1297–1300, 1990.

[14] C. Hagmann et al. Results from a high sensitivity search for cosmic axions. *Phys. Rev. Lett.*, 80:2043–2046, 1998, astro-ph/9801286.

[15] Stephen J. Asztalos et al. Large scale microwave cavity search for dark matter axions. *Phys. Rev.*, D64:092003, 2001.

[16] N. Du et al. A Search for Invisible Axion Dark Matter with the Axion Dark Matter Experiment. *Phys. Rev. Lett.*, 120(15):151301, 2018, 1804.05750.

[17] L. Zhong et al. Results from phase 1 of the HAYSTAC microwave cavity axion experiment. *Phys. Rev.*, D97(9):092001, 2018, 1803.03690.

[18] V. Anastassopoulos et al. New CAST Limit on the Axion-Photon Interaction. *Nature Phys.*, 13:584–590, 2017, 1705.02290.

[19] Igor Irastorza et al. The International Axion Observatory IAXO. Letter of Intent to the CERN SPS committee. 2013.

[20] E. Armengaud et al. Conceptual Design of the International Axion Observatory (IAXO). *JINST*, 9:T05002, 2014, 1401.3233.

[21] G. Vasilakis, J. M. Brown, T. W. Kornack, and M. V. Romalis. Limits on new long range nuclear spin-dependent forces set with a K - He-3 co-magnetometer. *Phys. Rev. Lett.*, 103:261801, 2009, 0809.4700.

[22] Georg Raffelt. Limits on a CP-violating scalar axion-nucleon interaction. *Phys. Rev.*, D86:015001, 2012, 1205.1776.

[23] B. R. Heckel, W. A. Terrano, and E. G. Adelberger. Limits on Exotic Long-Range Spin-Spin Interactions of Electrons. *Phys. Rev. Lett.*, 111(15):151802, 2013.

[24] W. A. Terrano, E. G. Adelberger, J. G. Lee, and B. R. Heckel. Short-range spin-dependent interactions of electrons: a probe for exotic pseudo-Goldstone bosons. *Phys. Rev. Lett.*, 115(20):201801, 2015, 1508.02463.

[25] A. A. Geraci et al. Progress on the ARIADNE axion experiment. *Springer Proc. Phys.*, 211:151–161, 2018, 1710.05413.

[26] R. Cameron et al. Search for nearly massless, weakly coupled particles by optical techniques. *Phys. Rev.*, D47:3707–3725, 1993.

[27] Cecile Robilliard, Remy Battesti, Mathilde Fouche, Julien Mauchain, Anne-Marie Sautivet, Francois Amiranoff, and Carlo Rizzo. No light shining through a wall. *Phys. Rev. Lett.*, 99:190403, 2007, 0707.1296.

[28] Aaron S. Chou, William Carl Wester, III, A. Baumbaugh, H. Richard Gustafson, Y. Irizarry-Valle, P. O. Mazur, Jason H. Steffen, R. Tomlin, X. Yang, and J. Yoo. Search for axion-like particles using a variable baseline photon regeneration technique. *Phys. Rev. Lett.*, 100:080402, 2008, 0710.3783.

[29] A. Afanasev, O. K. Baker, K. B. Beard, G. Biallas, J. Boyce, M. Minarni, R. Ramdon, M. Shinn, and P. Slocum. New Experimental limit on Optical Photon Coupling to Neutral, Scalar Bosons. *Phys. Rev. Lett.*, 101:120401, 2008, 0806.2631.

[30] Klaus Ehret et al. New ALPS Results on Hidden-Sector Lightweights. *Phys. Lett.*, B689:149–155, 2010, 1004.1313.

[31] R. Ballou et al. New exclusion limits on scalar and pseudoscalar axionlike particles from light shining through a wall. *Phys. Rev.*, D92(9):092002, 2015, 1506.08082.

[32] P. Sikivie, N. Sullivan, and D. B. Tanner. Proposal for Axion Dark Matter Detection Using an LC Circuit. *Phys. Rev. Lett.*, 112(13):131301, 2014, 1310.8545.

[33] Yonatan Kahn, Benjamin R. Safdi, and Jesse Thaler. Broadband and Resonant Approaches to Axion Dark Matter Detection. *Phys. Rev. Lett.*, 117(14):141801, 2016, 1602.01086.

[34] Maximiliano Silva-Feaver et al. Design Overview of DM Radio Pathfinder Experiment. *IEEE Trans. Appl. Supercond.*, 27(4):1400204, 2017, 1610.09344.

[35] Peter W. Graham and Surjeet Rajendran. Axion Dark Matter Detection with Cold Molecules. *Phys. Rev.*, D84:055013, 2011, 1101.2691.

[36] Dmitry Budker, Peter W. Graham, Micah Ledbetter, Surjeet Rajendran, and Alex Sushkov. Proposal for a Cosmic Axion Spin Precession Experiment (CASPEr). *Phys. Rev.*, X4(2):021030, 2014, 1306.6089.

[37] R. Barbieri, C. Braggio, G. Carugno, C. S. Gallo, A. Lombardi, A. Ortolan, R. Pengo, G. Ruoso, and C. C. Speake. Searching for galactic axions through magnetized media: the QUAX proposal. *Phys. Dark Univ.*, 15:135–141, 2017, 1606.02201.

[38] P. Sikivie. Axion Dark Matter Detection using Atomic Transitions. *Phys. Rev. Lett.*, 113(20):201301, 2014, 1409.2806.

[39] V. V. Flambaum, H. B. Tran Tan, I. B. Samsonov, Y. V. Stadnik, and D. Budker. Resonant detection and production of axions with atoms. *Int. J. Mod. Phys.*, A33(31):1844030, 2018.

[40] Y. V. Stadnik, V. A. Dzuba, and V. V. Flambaum. Improved Limits on Axionlike-Particle-Mediated P , T - Violating Interactions between Electrons and Nucleons from Electric Dipole Moments of Atoms and Molecules. *Phys. Rev. Lett.*, 120(1):013202, 2018, 1708.00486.

[41] Katharine Kelley and P. J. Quinn. A Radio Astronomy Search for Cold Dark Matter Axions. *Astrophys. J.*, 845(1):L4, 2017, 1708.01399.

[42] Guenter Sigl. Astrophysical Haloscopes. *Phys. Rev.*, D96(10):103014, 2017, 1708.08908.

[43] Fa Peng Huang, Kenji Kadota, Toyokazu Sekiguchi, and Hiroyuki Tashiro. The radio telescope search for the resonant conversion of cold dark matter axions from the magnetized astrophysical sources. 2018, 1803.08230.

[44] Anson Hook, Yonatan Kahn, Benjamin R. Safdi, and Zhiquan Sun. Radio Signals from Axion Dark Matter Conversion in Neutron Star Magnetospheres. 2018, 1804.03145.

[45] Benjamin R. Safdi, Zhiquan Sun, and Alexander Y. Chen. Detecting Axion Dark Matter with Radio Lines from Neutron Star Populations. 2018, 1811.01020.

[46] Andrea Caputo, Carlos Peña Garay, and Samuel J. Witte. Looking for axion dark matter in dwarf spheroidal galaxies. *Phys. Rev.*, D98(8):083024, 2018, 1805.08780.

[47] João G. Rosa and Thomas W. Kephart. Stimulated Axion Decay in Superradiant Clouds around Primordial Black Holes. *Phys. Rev. Lett.*, 120(23):231102, 2018, 1709.06581.

[48] I. I. Tkachev. An Axionic Laser in the Center of a Galaxy? *Phys. Lett.*, B191:41–45, 1987.

[49] Thomas W. Kephart and Thomas J. Weiler. Stimulated radiation from axion cluster evolution. *Phys. Rev.*, D52:3226–3238, 1995.

[50] Luca Di Luzio, Federico Mescia, and Enrico Nardi. Redefining the Axion Window. *Phys. Rev. Lett.*, 118(3):031801, 2017, 1610.07593.

[51] A. R. Zhitnitsky. On Possible Suppression of the Axion Hadron Interactions. (In Russian). *Sov. J. Nucl. Phys.*, 31:260, 1980. [Yad. Fiz.31,497(1980)].

[52] Michael Dine, Willy Fischler, and Mark Srednicki. A Simple Solution to the Strong CP Problem with a Harmless Axion. *Phys. Lett.*, 104B:199–202, 1981.

[53] Prateek Agrawal, JiJi Fan, Matthew Reece, and Lian-Tao Wang. Experimental Targets for Photon Couplings of the QCD Axion. *JHEP*, 02:006, 2018, 1709.06085.

[54] Marco Farina, Duccio Pappadopulo, Fabrizio Rompineve, and Andrea Tesi. The photo-philic QCD axion. *JHEP*, 01:095, 2017, 1611.09855.

[55] Edward Witten. Some Properties of O(32) Superstrings. *Phys. Lett.*, 149B:351–356, 1984.

[56] Peter Svrcek and Edward Witten. Axions In String Theory. *JHEP*, 06:051, 2006, hep-th/0605206.

[57] Asimina Arvanitaki, Savas Dimopoulos, Sergei Dubovsky, Nemanja Kaloper, and John March-Russell. String Axiverse. *Phys. Rev.*, D81:123530, 2010, 0905.4720.

[58] Michele Cicoli. Axion-like Particles from String Compactifications. In *Proceedings, 9th Patras Workshop on Axions, WIMPs and WISPs (AXION-WIMP 2013): Mainz, Germany, June 24-28, 2013*, pages 235–242, 2013, 1309.6988.

[59] Matthew D. Schwartz. *Quantum Field Theory and the Standard Model*. Cambridge University Press, 2014.

[60] Edward W. Kolb and Michael S. Turner. The Early Universe. *Front. Phys.*, 69:1–547, 1990.

[61] SKA Whitepaper, https://www.skatelescope.org/wp-content/uploads/2014/03/SKA-TEL-SKO-0000308_SKA1_System_Baseline_v2_DescriptionRev01-part-1-signed.pdf.

[62] L. B. Newburgh et al. HIRAX: A Probe of Dark Energy and Radio Transients. *Proc. SPIE Int. Soc. Opt. Eng.*, 9906:99065X, 2016, 1607.02059.

[63] Philip Bull, Pedro G. Ferreira, Prina Patel, and Mario G. Santos. Late-time cosmology with 21cm intensity mapping experiments. *Astrophys. J.*, 803(1):21, 2015, 1405.1452.

[64] C. G. T. Haslam, C. J. Salter, H. Stoffel, and W. E. Wilson. A 408 MHz all-sky continuum survey. II. The atlas of contour maps. *Astron. Astrophys. Suppl. Ser.*, 47:1–142, 1982.

[65] Mario G. Santos et al. Cosmology with a SKA HI intensity mapping survey. 2015, 1501.03989.

[66] Adrian Liu and Max Tegmark. How well can we measure and understand foregrounds with 21 cm experiments? *Mon. Not. Roy. Astron. Soc.*, 419:3491–3504, 2012, 1106.0007.

[67] Marco Regis, Laura Richter, Sergio Colafrancesco, Stefano Profumo, W. J. G. de Blok, and M. Massardi. Local Group dSph radio survey with ATCA – II. Non-thermal diffuse emission. *Mon. Not. Roy. Astron. Soc.*, 448(4):3747–3765, 2015, 1407.5482.

[68] D. J. Fixsen et al. ARCADE 2 Measurement of the Extra-Galactic Sky Temperature at 3-90 GHz. *Astrophys. J.*, 734:5, 2011, 0901.0555.

[69] Nicolao Fornengo, Roberto A. Lineros, Marco Regis, and Marco Taoso. The isotropic radio background revisited. *JCAP*, 1404:008, 2014, 1402.2218.

[70] Robin Bähre et al. Any light particle search II —Technical Design Report. *JINST*, 8:T09001, 2013, 1302.5647.

[71] Alex Geringer-Sameth, Savvas M. Koushiappas, and Matthew Walker. Dwarf galaxy annihilation and decay emission profiles for dark matter experiments. *Astrophys. J.*, 801(2):74, 2015, 1408.0002.

[72] Vincent Bonnivard, Celine Combet, David Maurin, Alex Geringer-Sameth, Savvas M. Koushiappas, Matthew G. Walker, Mario Mateo, Edward W. Olszewski, and John I. Bailey III. Dark matter annihilation and decay profiles for the Reticulum II dwarf spheroidal galaxy. *Astrophys. J.*, 808(2):L36, 2015, 1504.03309.

[73] V. Bonnivard et al. Dark matter annihilation and decay in dwarf spheroidal galaxies: The classical and ultrafaint dSphs. *Mon. Not. Roy. Astron. Soc.*, 453(1):849–867, 2015, 1504.02048.

[74] Kohei Hayashi, Koji Ichikawa, Shigeki Matsumoto, Masahiro Ibe, Miho N. Ishigaki, and Hajime Sugai. Dark matter annihilation and decay from non-spherical dark halos in galactic dwarf satellites. *Mon. Not. Roy. Astron. Soc.*, 461(3):2914–2928, 2016, 1603.08046.

[75] Jason L. Sanders, N. Wyn Evans, Alex Geringer-Sameth, and Walter Dehnen. Indirect Dark Matter Detection for Flattened Dwarf Galaxies. *Phys. Rev.*, D94(6):063521, 2016, 1604.05493.

[76] N. W. Evans, J. L. Sanders, and A. Geringer-Sameth. Simple J-Factors and D-Factors for Indirect Dark Matter Detection. *Phys. Rev.*, D93(10):103512, 2016, 1604.05599.

[77] Julio F. Navarro, Carlos S. Frenk, and Simon D. M. White. The Structure of cold dark matter halos. *Astrophys. J.*, 462:563–575, 1996, astro-ph/9508025.

[78] Marco Cirelli, Gennaro Corcella, Andi Hektor, Gert Hutsi, Mario Kadastik, Paolo Panci, Martti Raidal, Filippo Sala, and Alessandro Strumia. PPPC 4 DM ID: A Poor Particle Physicist Cookbook for Dark Matter Indirect Detection. *JCAP*, 1103:051, 2011, 1012.4515. [Erratum: JCAP1210,E01(2012)].

[79] F. Yusef-Zadeh et al. Interacting Cosmic Rays with Molecular Clouds: A Bremsstrahlung Origin of Diffuse High Energy Emission from the Inner 2deg by 1deg of the Galactic Center. *Astrophys. J.*, 762:33, 2013, 1206.6882.

[80] P. C. Gregory and E. R. Seaquist. The nature of Cygnus X-3 radio outbursts from an analysis of radiofrequency spectra. *ApJ*, 194:715–723, 1974.

[81] B. Vollmer, W. Reich, and R. Wielebinski. Detection of a radio halo in the Virgo cluster. *Astron. Astrophys.*, 423:57–64, 2004, astro-ph/0404124.

[82] F. N. Owen, J. a Eilek, and N. E. Kassim. M87 at 90cm: a different picture. *Astrophys. J.*, 543:611, 2000, astro-ph/0006150.

[83] LJ Oldham and MW Auger. Galaxy structure from multiple tracers–ii. m87 from parsec to megaparsec scales. *Monthly Notices of the Royal Astronomical Society*, 457(1):421–439, 2016.

[84] Laura B. Newburgh et al. Calibrating CHIME, A New Radio Interferometer to Probe Dark Energy. *Proc. SPIE Int. Soc. Opt. Eng.*, 9145:4V, 2014, 1406.2267.

[85] Cyril Creque-Sarbinowski and Marc Kamionkowski. Searching for Decaying and Annihilating Dark Matter with Line Intensity Mapping. *Phys. Rev.*, D98(6):063524, 2018, 1806.11119.

[86] Philip Ilten, Yotam Soreq, Mike Williams, and Wei Xue. Serendipity in dark photon searches. *JHEP*, 06:004, 2018, 1801.04847.

[87] J. P. Lees et al. Search for a Dark Photon in e^+e^- Collisions at BaBar. *Phys. Rev. Lett.*, 113(20):201801, 2014, 1406.2980.

[88] Martin Bauer, Patrick Foldenauer, and Joerg Jaeckel. Hunting All the Hidden Photons. *JHEP*, 07:094, 2018, 1803.05466.

[89] Motoi Endo, Koichi Hamaguchi, and Go Mishima. Constraints on Hidden Photon Models from Electron g-2 and Hydrogen Spectroscopy. *Phys. Rev.*, D86:095029, 2012, 1209.2558.

[90] Jonathan Kozaczuk. Dark Photons from Nuclear Transitions. *Phys. Rev.*, D97(1):015014, 2018, 1708.06349.

[91] Kunio Kaneta, Hye-Sung Lee, and Seokhoon Yun. Portal Connecting Dark Photons and Axions. *Phys. Rev. Lett.*, 118(10):101802, 2017, 1611.01466.

[92] Kazunori Kohri, Takeo Moroi, and Kazunori Nakayama. Can decaying particle explain cosmic infrared background excess? *Phys. Lett.*, B772:628–633, 2017, 1706.04921.

[93] Ryuji Daido, Fuminobu Takahashi, and Norimi Yokozaki. Enhanced axion–photon coupling in GUT with hidden photon. *Phys. Lett.*, B780:538–542, 2018, 1801.10344.

[94] Oleg E. Kalashev, Alexander Kusenko, and Edoardo Vitagliano. Cosmic infrared background excess from axion-like particles, and implications for multi-messenger observations of blazars. 2018, 1808.05613.

[95] Maurizio Giannotti, Igor Irastorza, Javier Redondo, and Andreas Ringwald. Cool WISPs for stellar cooling excesses. *JCAP*, 1605(05):057, 2016, 1512.08108.